Supporting Information

A resilient platform for the discrete functionalization of gold surfaces based on N-heterocyclic carbene self-assembled monolayers

Joseph M. Palasz‡[a], Zhuoran Long‡[b], Jinhui Meng[c], Pablo E. Videla[b], H. Ray Kelly[b], Tianquan Lian[c], Victor S. Batista[b], Clifford P. Kubiak*[a]

‡ Authors contributed equally to this work

* Corresponding author –

Clifford P. Kubiak – Email: ckubiak@ucsd.edu

Author affiliations

[a] Department of Chemistry and Biochemistry, University of California, San Diego, 9500 Gilman Drive, MC 0358, La Jolla, California, USA

[b]Department of Chemistry and Energy Sciences Institute, Yale University, 225 Prospect Street, New Haven, Connecticut 06520, USA

[c]Department of Chemistry, Emory University, 1515 Dickey Drive Northeast, Atlanta, Georgia 30322, USA

Contents

Synthetic Protocols

Synthesis of N^3,N^4-di-*tert*-butylpyridine-3,4-diamine

To a Teflon capped tube flask, 3,4-dibromopyridine (4.6 g, 19 mmol), sodium tert-butoxide (4.11 g, 42.8 mmol) and toluene (40 mL) were added and stirred vigorously. Separately, in a 20mL glass vial, palladium acetate (94 mg, 0.42 mmol), 1,3-Bis(2,6-diisopropylphenyl)imidazolium chloride (358 mg, 0.842 mmol) and sodium tert-butoxide (205 mg, 2.13 mmol) were stirred in toluene (10 ml) at room temperature. After 20 minutes the palladium mixture was added to the tube flask, followed by 2-methylpropan-2-amine (20 ml, 0.19 mol). The flask was then sealed and brought to 110C. After 5 days the mixture was cooled to room temperature, filtered over celite and rinsed with DCM. The resulting filtrate was dried in vacuo and purified by flash chromatography (solvent gradient 100% DCM to 30% MeOH in DCM). The main fraction was collected, dried in vacuo and the resulting dark brown oil was used without further purification.

Synthesis of 1,3-di-*tert*-butyl-3*H*-imidazo[4,5-c]pyridin-1-ium chloride - [PyNHC-H]PF_6

To a 100 mL flask, the product mixture from the previous reaction containing the diamine, NH_4Cl (5 g) and triethyl orthoformate (20 mL) were added. The mixture was stirred vigorously and brought to a reflux (140 C). After 12 hours the mixture was cooled, and the solvent evaporated in vacuo. The residual solid was resuspended in methanol, followed by the addition of a saturated solution of aqueous KPF_6, which resulted in the formation of a cream precipitate. The aqueous mixture was extracted with DCM (3x, 20 mL) and the organic layers collected, dried over $MgSO_4$, evaporated in vacuo, resulting in an off white solid of **[PyNHC-H]PF_6**. (4.58 g, 88% yield from 3,4-dibromopyridine) ^{1}H NMR (400 MHz, CD_3CN) δ 9.47 (d, J = 1.0 Hz, 1H), 8.71 (d, J = 5.9 Hz, 1H), 8.61 (s, 1H), 8.06 (dd, J = 5.9, 1.0 Hz, 1H), 1.82 (dd, J = 15.8, 1.0

Hz, 18H). ^{13}C NMR (100 MHz, CD_3CN) δ 144.76, 139.79, 139.35, 136.92, 129.24, 111.00, 62.61, 62.37, 28.18, 27.80. ESI-MS (m/z) $[M]^-$ 232.16 (found) $[C_{14}H_{22}N_3]^-$ 232.18 (calc.)

Synthesis of $[(PyNHC)_2Au]PF_6$

Under an atmosphere of nitrogen [PyNHC-H]PF_6 (353 mg, 0.93 mmol) and LiHMBS (380 mg, 2.27 mmol) were mixed in a dried scintillation vial with 10 mL THF for one hour at room temperature. The solution was filtered and added to a roundbottom containing AuCl(THT) in THF and the mixture was stirred for another 24 hours in the dark. The mixture was then filtered over a pad of celite and rinsed with DCM and methanol. The resulting filtrate was dried under vacuum, redissolved in a small amount of acetone and precipitated by the addition of hexanes. For monolayer preparation the compound was further purified by flash chromatography (silica gel, 100% DCM to 30% MeOH in DCM). The primary fraction was $[(PyNHC)_2Au]PF_6$ (254 mg, 33% yield) ^1H NMR (500 MHz, $CDCl_3$) δ 9.37 (s, 2H), 8.46 (d, J = 6.0 Hz, 2H), 7.96 (dd, J = 6.0, 1.0 Hz, 2H), 2.08 (d, J = 17.5 Hz, 36H). ESI-MS (m/z) $[M+H^+]$: 660.4 (found) $[C_{28}H_{43}AuN_6^+]$ 660.3 (calc.) AP-CI HR-MS (m/z) $[M+MeOH]^-$ 689.33 (found) $[C_{28}H_{42}AuN_6+CH_4O]^+$ 689.324 (calc.)

Spectroscopic Experimental Information

PM-IRRAS measurements

PM-IRRAS spectra were collected using a Bruker Invenio FTIR spectrometer with a PMA-37 accessory module fitted with a MCT optical detector, a Hinds instruments PEM-90 photoelastic modulator operating with half wave retardation at 2500 cm^{-1} for fingerprint and CO regions, and 3000 cm^{-1} for detecting the C-H region. A GWC instruments synchronous sampling demodulator phase adjusted to match the PEM using an Siglent oscilloscope was used to extract the (P-S)

interferogram. Samples were collected with an 80 degree angle of incidence with a spectral resolution of 4 cm^{-1} and a 1 hour acquisition time. The (P-S) and (P+S) spectra were collected simultaneously, processed using the formula (P-S)/(P+S) to obtain the PM-IRRAS spectrum, which was then baselined using a rubberband correction within the Bruker Opus software suite to remove the second order Bessel function.

Raman measurements

For Raman measurements, a home-built system with 633 nm He-Ne laser (Thorlabs HNL210LB) and a 10X microscope objective (10X Olympus Plan Achromat Objective, 0.25 NA, 10.6 mm WD, from Thorlabs, RMS10X) was used. The sample was fixed at the home-built stage and the Raman signal was collected by a spectrograph (Shamrock, Andor, 600 l/m grating) and detected by an electron-multiplied charge coupled device (Newton EMCCD, Andor).

XPS measurements

Chemical composition of the monolayer PyNHC on Au samples were obtained by XPS on a Kratos Axis Ultra DLD system at a take-off angle of 0° relative to the surface normal. An Al Kα source (hν = 1,486.6 eV) was used with a pass energy of 40 eV for the narrow scan of core levels with a step size of 0.05 eV. The spectral fitting was conducted using CasaXPS analysis software. Atomic ratios were calculated by integration of a survey sweep XPS spectrum using the N 1s region and Au $4f_{5/2}$ peak and scaled using the library of sensitivity factors included with CasaXPS software suite. The sensitivity factors used for the N 1s, Au $4d_{5/2}$ and F 1s peaks were 1.8, 11.74, and 4.43 respectively as taken from the library of relative sensitivity factors included in CasaXPS. Spectrum referenced to Au 4f 7/2 set to a binding energy of 84 eV and verified

using the peak of adventitious carbon at 284.6 eV, confirming that the observed Au signal corresponds to predominantly Au(0).

Computational Details

Details of computational methods

In the cluster model of the surface-bound PyNHC, the gold cluster representing the Au (111) surface consisted of 21 Au atoms in two layers, with 15 Au atoms in the top layer and 6 in the bottom layer. All Au atoms were frozen except three at the center of the top layer. DFT calculations for cluster models and corresponding free molecules utilized the Gaussian 16, Revision C.01 package[1] with the ωB97X-D exchange-correction functional[2]. The Def2SVP basis set and effective core potential (ECP)[3] was used for the Au atoms and the 6-31G(d,p) basis set[4,5] was used for all the other atoms. Geometry optimization and vibrational frequency analysis were performed in vacuum, followed by single point energy calculations with the Polarizable Continuum Model (PCM)[6] implicit solvent of acetonitrile. The electrostatic potential-derived Merz-Singh-Kollman (MSK) charges were calculated with the UFF radii and default fitting parameters in Gaussian 16 package for charge analysis. All computational spectra frequencies are scaled by a factor of 0.949[8].

Slab models of PyNHC bound to a gold (111) surface under periodic boundary conditions were built to examine the PyNHC binding modes and verify cluster models. DFT calculations were performed with the Vienna Ab Initio Simulation Package (VASP) 5.4.1 package[9-13], using the Perdew-Berke-Ernzerhof (PBE) exchange-correlation functional[14] with Grimme's DFT-D3 dispersion correction (Becke-Johnson damping)[15,16] and the projector-augmented wave (PAW) method[13,17] with a 450 eV cutoff. First order Methfessel-Paxton smearing[18] was used with σ =

0.2. To construct the slab, we conducted a bulk optimization of the Au fcc unit cell consisting of 4 Au atoms with a 21×21×21 Monkhorst-Pack (MP) k-point grid centered at the Γ point, 10^{-6} eV SCF convergence criterion, 10^{-5} eV geometry optimization criterion, and the projection operators evaluated in the reciprocal space. Based on the 4.101 Å unit cell vector length from the bulk optimization, we built a slab model in a hexagonal box with $a = b$ =14.498 Å and c = 35 Å with five Au atoms in the a and b direction and four layers in the c direction in the slab. This box dimension gave a surface coverage of 0.0055 $Å^{-2}$, and a vacuum space of > 27 Å in the z direction between the slabs (> 18 Å with a standing PyNHC). Geometry optimizations of slab models were performed with a 3×3×1 MP k-point grid centered at the Γ point, 10^{-5} eV SCF convergence criterion, a 0.01 eV/Å geometry optimization convergence criterion, fully automatic optimization of projection operators in real space, and all other settings the same as the bulk optimization, followed by single point energy calculations on the optimized geometries with a 5×5×1 MP k-point grid centered at the Γ point. The geometry optimization and single point energy calculation of the PyNHC carbene was done at the Γ point with a box of 25×25×25 $Å^3$, with all other settings the same as slab models. The volume-based Atoms-in-Molecules (AIM) charges were calculated with the Bader Charge Analysis code[19-22] for periodic slab models to benchmark results from cluster models.

Thermodynamic corrections for reactions in the solution phase

For cluster models, gas phase (vacuum) DFT optimizations and frequency calculations were performed to obtain the Gibbs Free energy ($G_g = E_g + E_{corr}$, where E_g is the gas phase electronic energy and E_{corr} is the thermodynamic correction) at the optimized geometry. Thermodynamic corrections (E_{corr}) were computed at temperature T = 298.15 K and pressure p_g^0

= 1 atm utilizing the rigid rotor-harmonic oscillator approximation. To convert the gas phase free energy changes to solution phase ones, a single point calculation was performed using the optimized geometry in the Polarizable Continuum Model (PCM) implicit solvent of acetonitrile (MeCN), to obtain the solution phase electronic energy E_{sol}. A Born-Haber cycle was utilized to obtain the free energy change for the reaction in the implicit solvent:

$$\begin{array}{ccc} \mathrm{R}(g) & \rightarrow & \mathrm{P}(g) \\ \downarrow & & \downarrow \\ \mathrm{R}(sol) & \rightarrow & \mathrm{P}(sol) \end{array}$$

The gas phase reaction free energy change is:

$$\Delta_r G_g = G_{\mathrm{P},g} - G_{\mathrm{R},g}$$

The solvation energies for the reactant and the product are approximated as:

$$\Delta G_{i,\,solv} = E_{i,sol} - E_{i,g} \qquad i = \mathrm{R},\, \mathrm{P}$$

The reaction free energy change in the solution phase is:

$$\Delta_r G_{sol} = \Delta_r G_g + \Delta G_{\mathrm{P},solv} - \Delta G_{\mathrm{R},solv} = E_{\mathrm{P},sol} - E_{\mathrm{R},sol} + E_{\mathrm{P},corr} - E_{\mathrm{R},corr}$$

Besides the entropy corrections, we also need to correct the free energy change to the thermodynamic standard state. The gas phase thermodynamic standard state corresponds to a concentration of $c_g^0 = p/(RT)$ = 0.04087 mol/L (R: the gas constant), while the solution phase standard state concentration is c_{sol}^0 = 1 mol/L. For an example reaction will all reactants and products in solution phase

$$\mathrm{A}^a(sol) + \mathrm{B}^b(sol) \rightarrow \mathrm{C}^c(sol) + \mathrm{D}^d(sol)$$

the solution phase free energy change $\Delta_r G_{sol}^0$ should be calculated from the gas phase free energy change $\Delta_r G_{sol}$ using the equation:

$$\Delta_r G^0_{sol} = \Delta_r G_{sol} + RT\ln Q_{sol}$$

with the reaction quotient Q_{sol} being

$$Q_{sol} = \frac{\left(\frac{p^0_{\mathrm{C},sol}}{p^0_{\mathrm{C},g}}\right)^c \left(\frac{p^0_{\mathrm{D},sol}}{p^0_{\mathrm{D},g}}\right)^d}{\left(\frac{p^0_{\mathrm{A},sol}}{p^0_{\mathrm{A},g}}\right)^a \left(\frac{p^0_{\mathrm{B},sol}}{p^0_{\mathrm{B},g}}\right)^b} = \frac{\left(\frac{c^0_{\mathrm{C},sol}}{c^0_{\mathrm{C},g}}\right)^c \left(\frac{c^0_{\mathrm{D},sol}}{c^0_{\mathrm{D},g}}\right)^d}{\left(\frac{c^0_{\mathrm{A},sol}}{c^0_{\mathrm{A},g}}\right)^a \left(\frac{c^0_{\mathrm{B},sol}}{c^0_{\mathrm{B},g}}\right)^b} = \left(\frac{c^0_{sol}}{c^0_g}\right)^{c+d-a-b}$$

Therefore, the correction factor is:

$$RT\ln Q_{sol} = 1.89(c + d - a - b)\ [\mathrm{kcal/mol}]$$

where $c + d - a - b$ is the stoichiometry change of solution phase species.

In our case, the chemical equation for $[(\mathrm{PyNHC})\mathrm{Au}]^+$ binding is:

$$[(\mathrm{PyNHC})\mathrm{Au}]^+ (\mathrm{sol}) + \mathrm{Au}\ (\mathrm{s}) \rightarrow [(\mathrm{PyNHC})\mathrm{Au}]\text{-}\mathrm{Au}^+ (\mathrm{s})$$

where Au(s) represents the gold surface. There is only one reactant in the solution phase, i.e., $c + d - a - b = -1$, so a correcting factor of -1.89 kcal/mol should be added to the free energy change.

For binding [(PyNHC)Au]-L to the surface:

$$[(\mathrm{PyNHC})\mathrm{Au}]\text{-}\mathrm{L}\ (\mathrm{sol}) + \mathrm{Au}\ (\mathrm{s}) \rightarrow [(\mathrm{PyNHC})\mathrm{Au}]\text{-}\mathrm{Au}^+ (\mathrm{s}) + \mathrm{L}^-\ (\mathrm{sol})$$

where L^- can be PyNHC, Cl^-, or OH^-. The stoichiometry change is $c + d - a - b = 0$, so the correcting factor is 0.

For situation where the solvent MeCN is the ligand, the reaction becomes:

$$[(\mathrm{PyNHC})\mathrm{Au}]\text{-}\mathrm{MeCN}^+ (\mathrm{sol}) + \mathrm{Au}\ (\mathrm{s}) \rightarrow [(\mathrm{PyNHC})\mathrm{Au}]\text{-}\mathrm{Au}^+ (\mathrm{s}) + \mathrm{MeCN}\ (\mathrm{l})$$

The concentration of solvent (MeCN) can be calculated from its liquid state density ρ_l[23]:

$$c_l = \frac{\rho_l}{M} = \frac{782.5\ \text{g/L}}{41.053\ \text{g/mol}} = 19.1\ \text{mol/L}$$

where M is the molar mass of MeCN. The correction factor will be:

$$RT\ln Q = RT\ln\frac{c_{\text{MeCN}}}{c_{sol}^0} = 1.75\ \text{kcal/mol}$$

Validation of the cluster model

We examined the reliability of the cluster model by comparing the binding energy of the PyNHC carbene to the gold surface with an adatom between the cluster model and slab model (Figure S-1). The cluster model gives internal energy change ΔE = -71.8 kcal/mol and ΔG = -57.8 kcal/mol. The slab model gives ΔE = -66.7 kcal/mol. Considering the vast difference between the two models and computational methods, the binding energies from these two models match well with each other.

DFT charge analysis

The charge analysis results are summarized in Table S-1. Charges on the PyNHC moiety, Au clusters or slabs were obtained by summing over composing atoms. In the homoleptic $[(\text{PyNHC})_2\text{Au}]^+$ precursor, the positive charge is delocalized on both PyNHC moieties (0.643 *e* and 0.637 *e*) while the Au atom is negatively charged (-0.280 *e*). This reflects the strong electron donor properties of the NHC ligands, which result in an electron rich Au center. In the positively charged cluster model [(PyNHC)Au]-Cluster$^+$, the Au adatom is positively charged (0.206 *e*), indicating that the Au still has positive charge density. And the net positive charge is mostly delocalized in the Au cluster. Adding one electron to the system will slightly reduce the Au

adatom but it is still positively charged (0.117 e in [(PyNHC)Au]-Cluster). The slab model also predicts a positively charged Au adatom (0.088 e), consistent with the neutral cluster model.

Calculation of PM-IRRAS spectra

Polarization modulation infrared reflection absorption spectroscopy (PM-IRRAS) is a surface-sensitive technique useful for determining the average binding orientation for absorbed molecules on conducting surfaces. Due to the selection rules of metal surfaces, the intensity of PM-IRRAS spectral lines is dependent on the angle between the transition dipole moment of the vibrational modes and the surface normal. As such, only signals with transition dipole moments with amplitude normal to the surface are enhanced. By comparing the PM-IRRAS amplitudes with the corresponding amplitudes for isotropic (i.e., bulk) environments, the average molecular orientation of SAMs can be determined.

The calculation of DFT-based PM-IRRAS spectra was based on our previous work in simulating SFG spectroscopy. In brief, the PM-IRRAS intensity is given by

$$I_{PM-IRRAS}(\omega_{IR}) \propto \sum_n \frac{A_n^{zz}}{(\omega_n - \omega_{IR})^2 + \left(\frac{\Gamma_n}{2}\right)^2},$$

where the sum runs over all the vibrational normal modes with frequency ω_n, A_n^{zz} represents the PM-IRRAS response amplitude for normal mode n, and Γ_n is a phenomenological damping constant. The amplitude A_n^{zz} is related to the transition dipole moments by

$$A_n^{zz} = \sum_{\alpha\beta} \langle R_{z\alpha} R_{z\beta} \rangle \mu_n^{\alpha} \mu_n^{\beta},$$

where μ_n^k ($k = x,y,z$) are the Cartesian components of the transition dipole moment for normal mode n, $\boldsymbol{R}(\psi,\theta,\phi)$ are Euler rotation matrices that superimpose the axes of the molecular coordinate system with those of the macroscopic laboratory coordinate system and where angular brackets represent ensemble averages over the angular orientational distribution. In the present work, the molecular coordinate system coincides with the laboratory coordinate system, and we assumed fixed orientational distribution, thus the PM-IRRAS amplitude is given by

$$A_n^{zz} = \left(\mu_n^z\right)^2.$$

Transition dipole moments were computed assuming a harmonic approximation as

$$\mu_n^z = \sqrt{\frac{\hbar}{2\omega_n}}\frac{\partial \mu_z}{\partial Q_n},$$

where μ_z is the molecular dipole moment and Q_n is the normal mode coordinate of the n-th vibrational mode.

PM-IRRAS spectra were simulated at the ωB97X-D level employing the cluster model of surface-bound PyNHC. Harmonic frequency calculations were performed on the optimized stationary points to obtain frequencies and dipole derivatives with respect to each normal mode. All harmonic frequencies were scaled by 0.949[8] to facilitate the comparison with experimental spectra and we set $\Gamma_n = 15\ cm^{-1}$ for all vibrational modes.

Supplemental Tables

Table S-1 DFT charge analysis of PyNHC

Model	System	PyNHC (*e*)	Au (*e*)	Ligand / Cluster (*e*)
Cluster (MSK charge)	$[(PyNHC)_2Au]^+$	0.643	-0.280	0.637
	$[(PyNHC)Au]$-$Cluster^+$	0.055	0.206	0.739
	[(PyNHC)Au]-Cluster	0.005	0.117	-0.122
	$[(PyNHC)Au]$-$Cluster^-$	0.006	-0.140	-0.866
	[(PyNHC)Au]-Cl	0.317	0.128	-0.445
Periodic slab (AIM charge)	[(PyNHC)Au]-Slab	0.309	0.088	-0.398
	[(PyNHC)Au]-Cl	0.296	0.259	-0.554

Table S-2 Vibrational modes studied in SERS and PM-IRRAS and their assignments

Assignment	**SERS**	**PM-IRRAS**
C=N stretch (pyridine)	1593 cm^{-1}	1593 cm^{-1}
C-H bend (tBu)	1464 cm^{-1}	1464 cm^{-1}
C-N stretch (C4,5-N)		1373 cm^{-1}
C-N stretch (C2-N)	1346 cm^{-1}	

Supplemental Figures

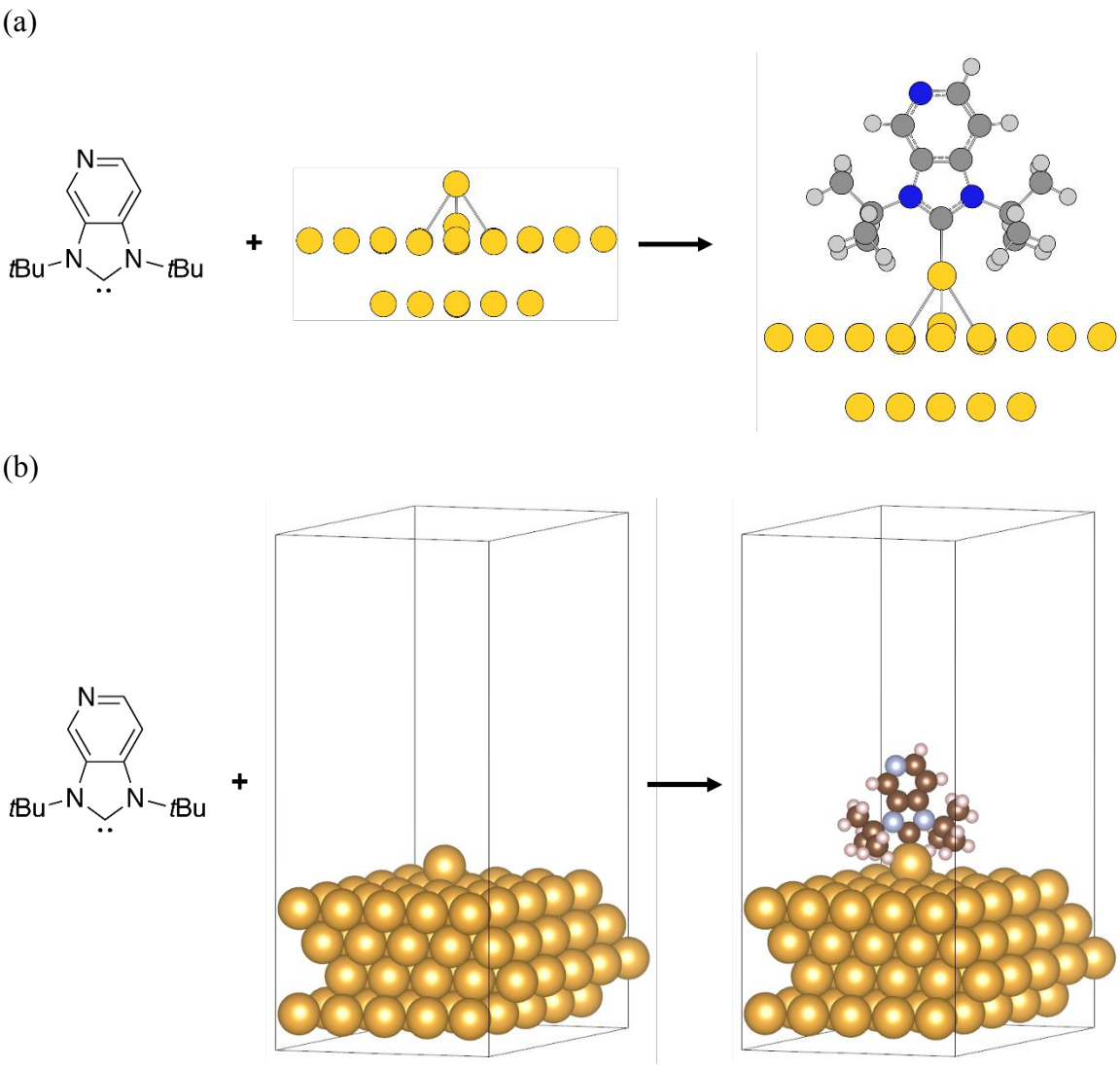

Figure S-1. Schematic representation of PyNHC carbene binding to an adatom on the Au (111) surface with (a) the cluster model and (b) the slab model. Atoms are indicated by color for the cluster model by yellow (Au), blue (N), grey (C) and white (H). Atoms are indicated by color for the slab model by yellow (Au), pale blue (N), brown (C) and white (H).

(a) 0 kcal/mol (reference)

(b) 0.03 kcal/mol

Figure S-2. Geometries and energies for two azimuthal orientations of the PyNHC molecule on the Au adatom. (a) is the same system as Figure 2(a). Atoms are indicated by color for the slab model by yellow (Au), pale blue (N), brown (C) and white (H).

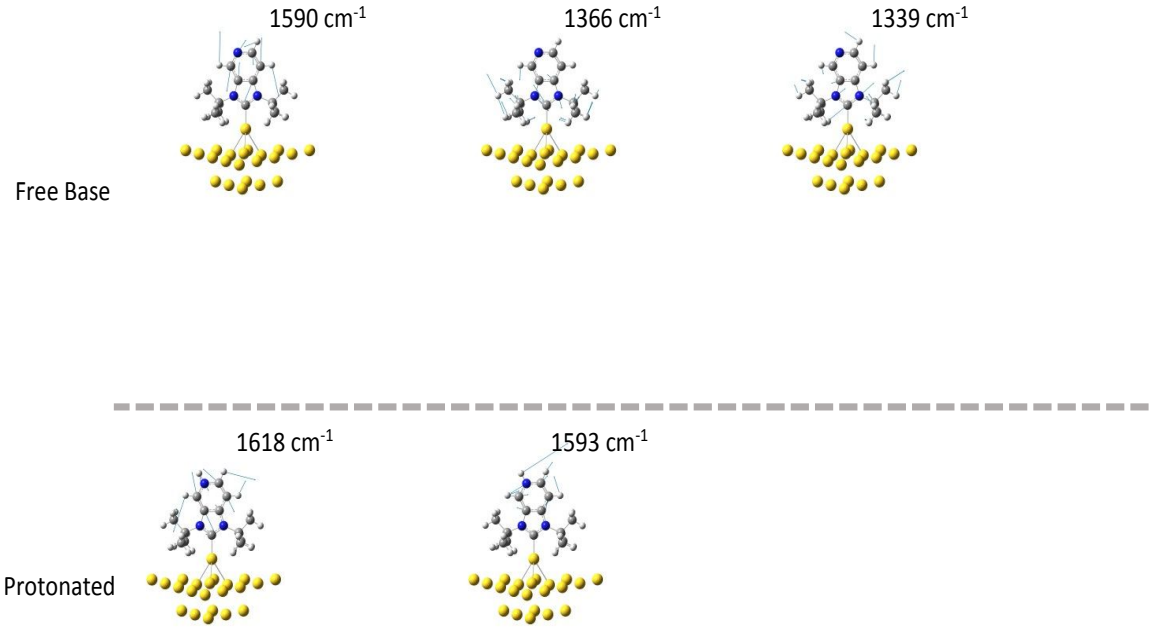

Figure S-3: Vector representations of atom displacements in select normal modes for the free base PyNHC-SAM (Top) and the two C=C modes which occur in the protonated SAM (Bottom). Atoms are indicated by color following the scheme yellow (Au), blue (N), grey (C) and white (H)

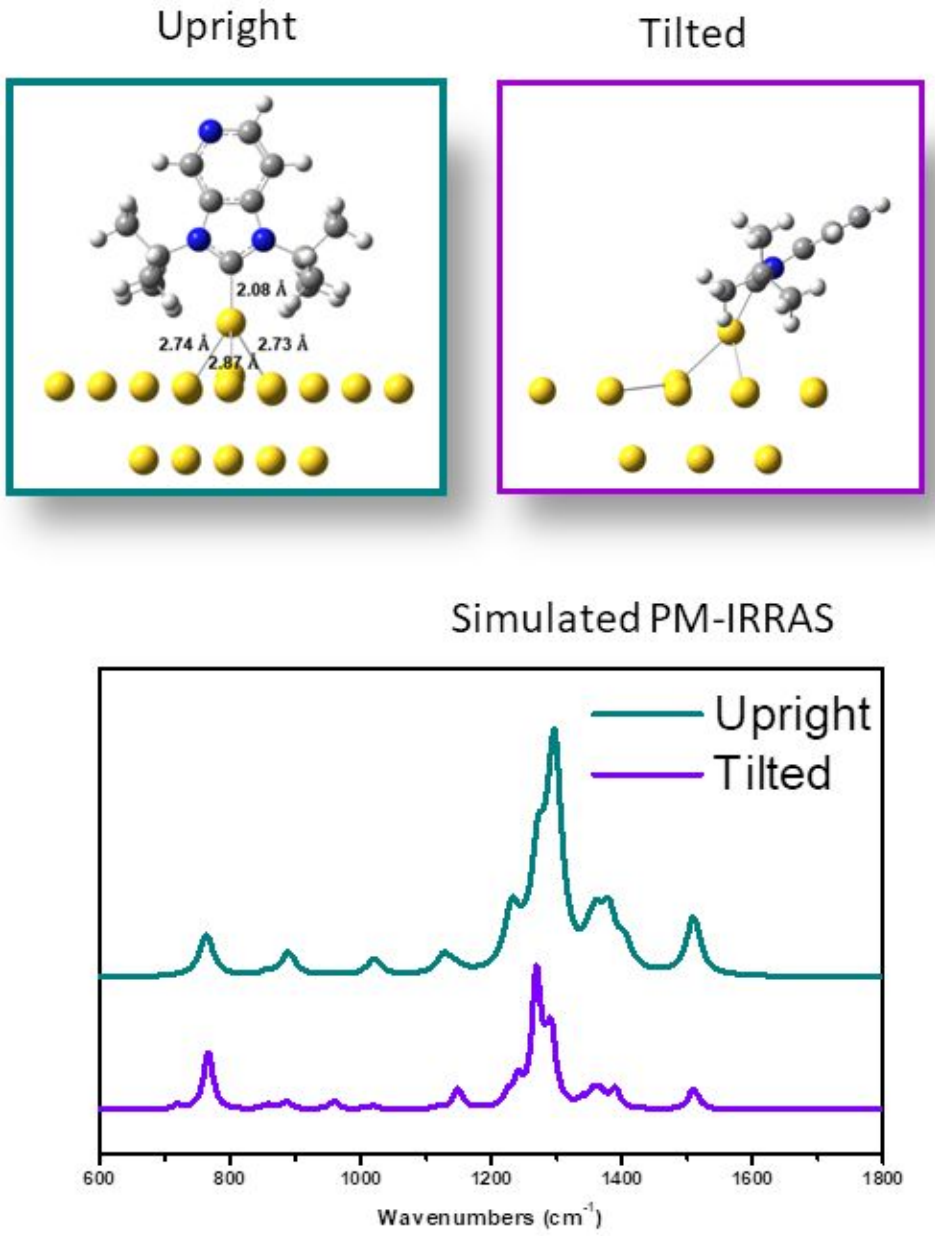

Figure S-4: Binding orientations used for simulating PM-IRRAS spectra for upright and tilted geometries (top) and calculated spectra using PM-IRRAS selection rules for both plausible binding modes (bottom). Atoms in DFT models are indicated by color following the scheme yellow (Au), blue (N), grey (C) and white (H)

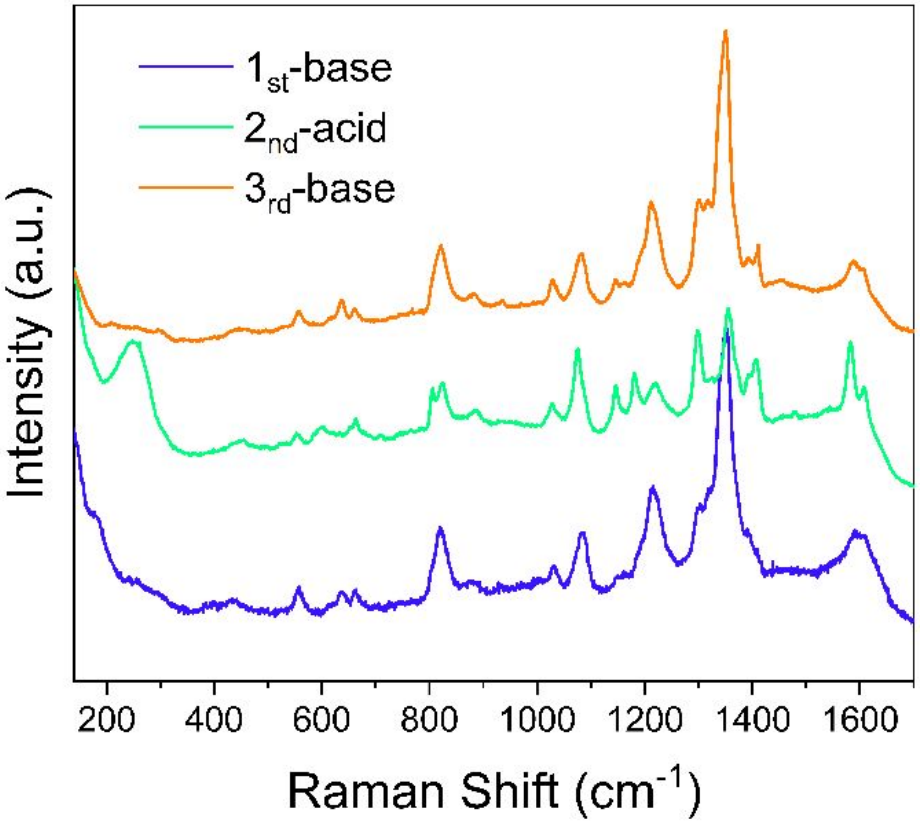

Figure S-5. SERS spectra of SAM on Au substrate. Different colors represent the different times of treatment in different solutions: blue line— the first treatment with basic solution to prepare free-base monolayers (0.1 M NaOH), green line—the second treatment with acidic solution (50 mM H_2SO_4), orange line—the third treatment with basic solution (0.1 M NaOH).

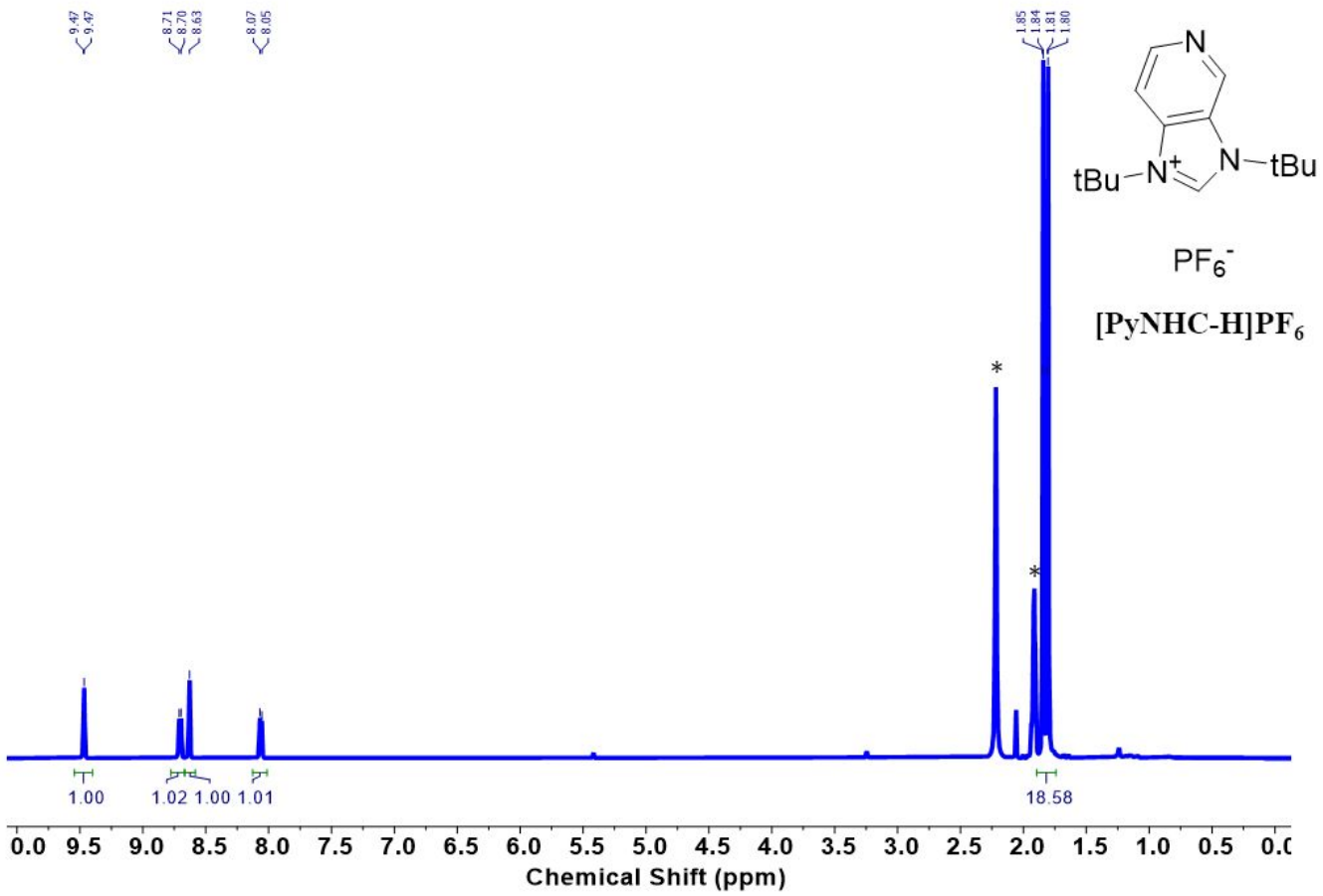

Figure S-6: ^{1}H NMR of [PyNHC-H]PF_6 in D_3-MeCN. *indicates residual peaks from adventitious H_2O and solvent.

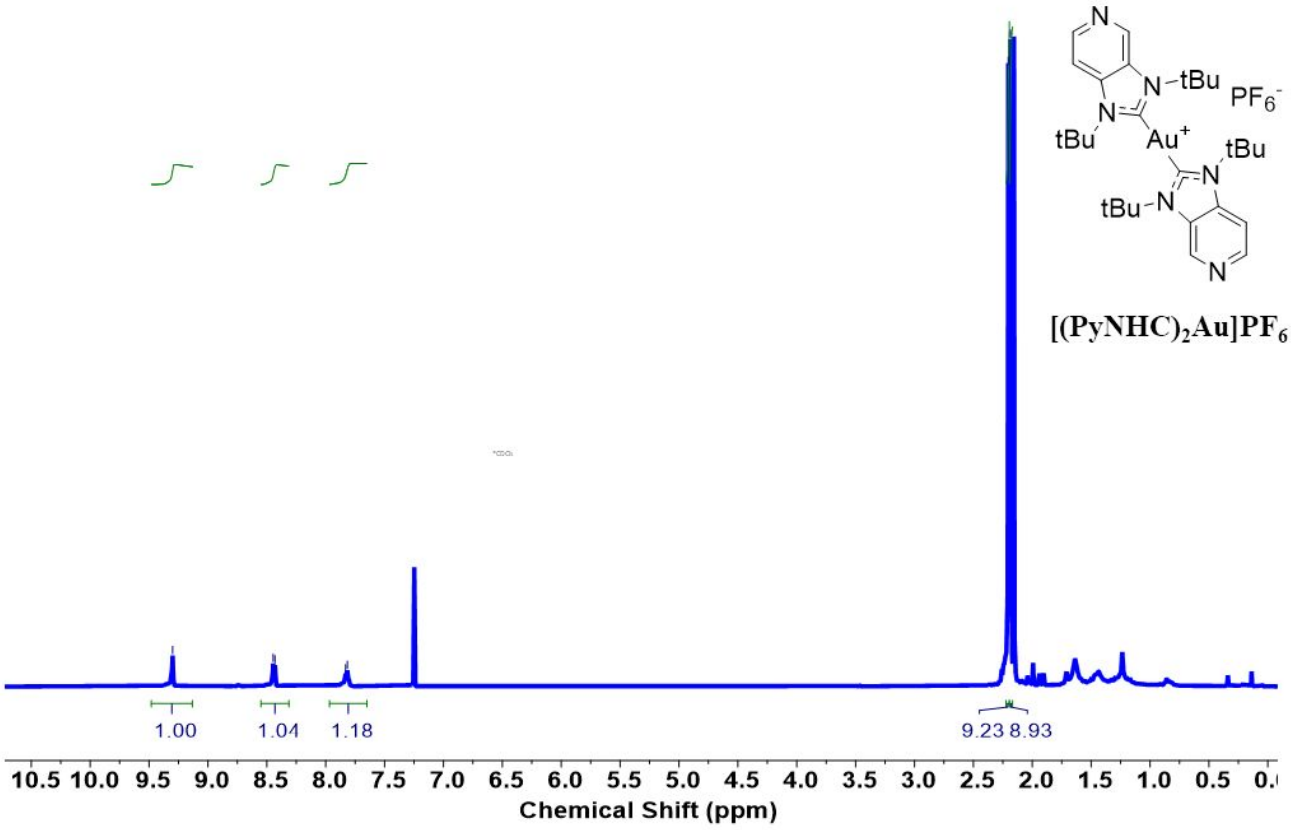

Figure S-7: ^{1}H NMR of $[(PyNHC)_2Au]PF_6$ in $CDCl_3$ from recrystallization from Acetone/Hexanes solvent mixture.

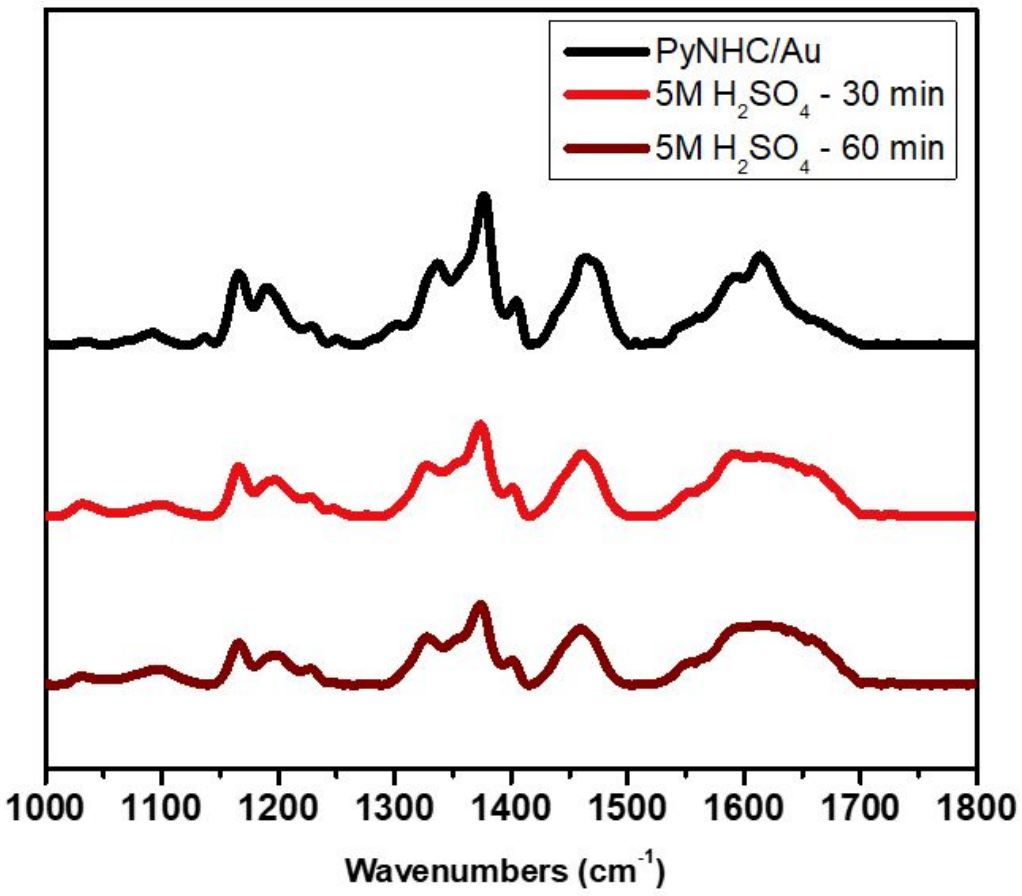

Figure S-8: PM-IRRAS spectra of PyNHC monolayers on gold slides freshly prepared (black trace) soaked in 5M H_2SO_4 (aq) for 30 minutes (red trace) and 60 minutes (burgundy trace).

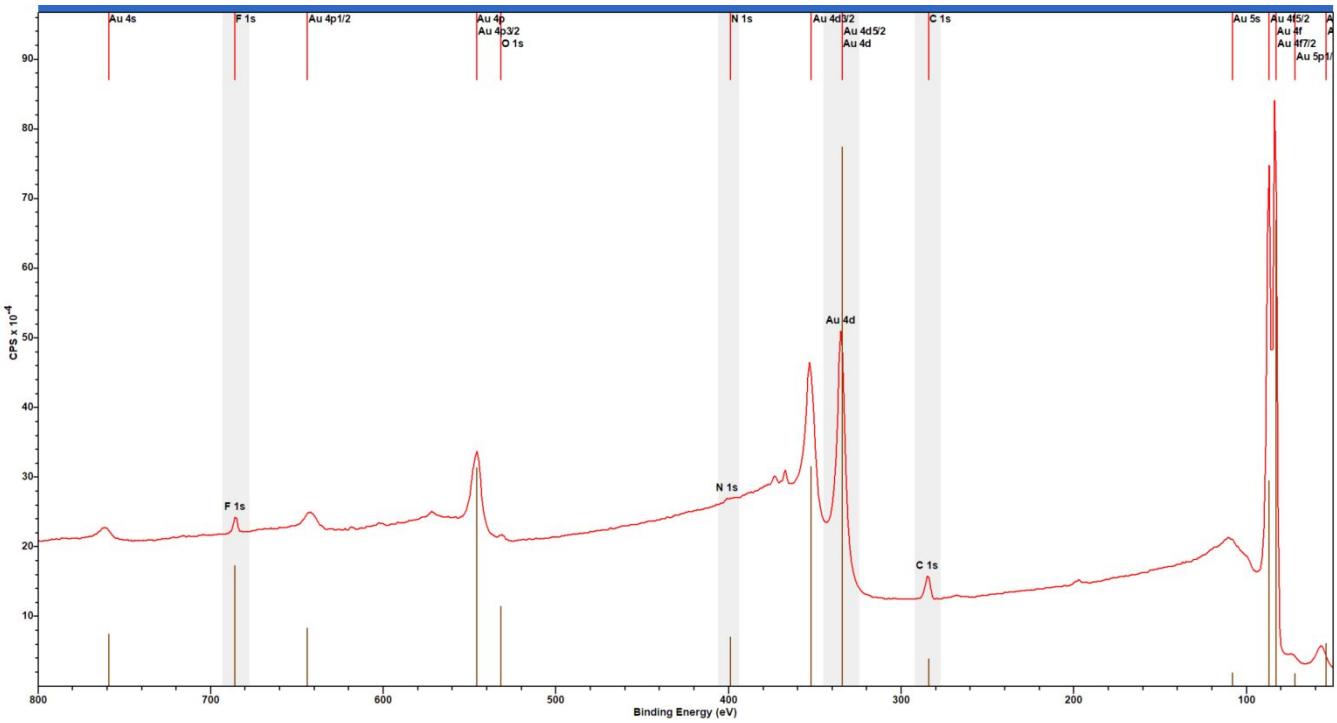

Figure S-9: XPS survey spectrum taken of PyNHC on Au with assigned transitions corresponding to Au, C, N and F marked with red ticks. Integrated regions used for fitting and atomic composition are shaded in grey. O

References

1 Gaussian 16 v. Rev. C.01 (Gaussian, Inc. Wallingford, CT, 2016).

2 Chai, J.-D. & Head-Gordon, M. Long-range corrected hybrid density functionals with damped atom–atom dispersion corrections. *Physical Chemistry Chemical Physics* **10**, 6615-6620 (2008). https://doi.org/10.1039/B810189B

3 Weigend, F. Accurate Coulomb-fitting basis sets for H to Rn. *Physical Chemistry Chemical Physics* **8**, 1057-1065 (2006). https://doi.org/10.1039/B515623H

4 Francl, M. M. *et al.* Self-consistent molecular orbital methods. XXIII. A polarization-type basis set for second-row elements. *The Journal of Chemical Physics* **77**, 3654-3665 (1982). https://doi.org/10.1063/1.444267

5 Hariharan, P. C. & Pople, J. A. The influence of polarization functions on molecular orbital hydrogenation energies. *Theoretica chimica acta* **28**, 213-222 (1973). https://doi.org/10.1007/BF00533485

6 Tomasi, J., Mennucci, B. & Cammi, R. Quantum Mechanical Continuum Solvation Models. *Chemical Reviews* **105**, 2999-3094 (2005). https://doi.org/10.1021/cr9904009

7 Miller, C. J. *et al.* PM-IRRAS and DFT investigation of the surface orientation of new Ir piano-stool complexes attached to Au(111). *Dalton Transactions* **51**, 17688-17699 (2022). https://doi.org/10.1039/D2DT02730E

8 Johnson III, R. D. *NIST Computational Chemistry Comparison and Benchmark Database, NIST Standard Reference Database Number 101*, <http://cccbdb.nist.gov/> (2022).

9 Kresse, G. & Furthmüller, J. Efficiency of ab-initio total energy calculations for metals and semiconductors using a plane-wave basis set. *Computational Materials Science* **6**, 15-50 (1996). https://doi.org/https://doi.org/10.1016/0927-0256(96)00008-0

10 Kresse, G. & Furthmüller, J. Efficient iterative schemes for ab initio total-energy calculations using a plane-wave basis set. *Physical Review B* **54**, 11169-11186 (1996). https://doi.org/10.1103/PhysRevB.54.11169

11 Kresse, G. & Hafner, J. Ab initio molecular dynamics for liquid metals. *Physical Review B* **47**, 558-561 (1993). https://doi.org/10.1103/PhysRevB.47.558

12 Kresse, G. & Hafner, J. Ab initio molecular-dynamics simulation of the liquid-metal--amorphous-semiconductor transition in germanium. *Physical Review B* **49**, 14251-14269 (1994). https://doi.org/10.1103/PhysRevB.49.14251

13 Kresse, G. & Joubert, D. From ultrasoft pseudopotentials to the projector augmented-wave method. *Physical Review B* **59**, 1758-1775 (1999). https://doi.org/10.1103/PhysRevB.59.1758

14 Perdew, J. P., Burke, K. & Ernzerhof, M. Generalized Gradient Approximation Made Simple. *Physical Review Letters* **77**, 3865-3868 (1996). https://doi.org/10.1103/PhysRevLett.77.3865

15 Grimme, S., Antony, J., Ehrlich, S. & Krieg, H. A consistent and accurate ab initio parametrization of density functional dispersion correction (DFT-D) for the 94 elements H-Pu. *The Journal of Chemical Physics* **132** (2010). https://doi.org/10.1063/1.3382344

16 Grimme, S., Ehrlich, S. & Goerigk, L. Effect of the damping function in dispersion corrected density functional theory. *Journal of Computational Chemistry* **32**, 1456-1465 (2011). https://doi.org/https://doi.org/10.1002/jcc.21759

17 Blöchl, P. E. Projector augmented-wave method. *Physical Review B* **50**, 17953-17979 (1994). https://doi.org/10.1103/PhysRevB.50.17953

18 Methfessel, M. & Paxton, A. T. High-precision sampling for Brillouin-zone integration in metals. *Physical Review B* **40**, 3616-3621 (1989). https://doi.org/10.1103/PhysRevB.40.3616

19 Henkelman, G., Arnaldsson, A. & Jónsson, H. A fast and robust algorithm for Bader decomposition of charge density. *Computational Materials Science* **36**, 354-360 (2006). https://doi.org/https://doi.org/10.1016/j.commatsci.2005.04.010

20 Sanville, E., Kenny, S. D., Smith, R. & Henkelman, G. Improved grid-based algorithm for Bader charge allocation. *Journal of Computational Chemistry* **28**, 899-908 (2007). https://doi.org/https://doi.org/10.1002/jcc.20575

21 Tang, W., Sanville, E. & Henkelman, G. A grid-based Bader analysis algorithm without lattice bias. *Journal of Physics: Condensed Matter* **21**, 084204 (2009). https://doi.org/10.1088/0953-8984/21/8/084204

22 Yu, M. & Trinkle, D. R. Accurate and efficient algorithm for Bader charge integration. *The Journal of Chemical Physics* **134** (2011). https://doi.org/10.1063/1.3553716

23 *CRC handbook of chemistry and physics*. 104 edn, (CRC Press, 2023).